Refractive Index of Lithium Fluoride
Ramp Compressed to 800 GPa

Introduction

The transition of an insulator to a metal (metallization) at high compression is generally the result of pressure-induced closure of the band gap.[1–4] Lithium fluoride's (LiF's) large-band-gap and ionic crystalline structure produces its uniquely high ultraviolet transmissivity. Two rare-gas solids, He and Ne, have anomalously high metallization pressures because of the predicted intershell band overlap, which is unique among monatomic materials.[5] LiF holds a rare position among binary compounds in that Li^+ and F^- are isoelectronic with He and Ne, respectively. Therefore, LiF is expected to have a uniquely high metallization pressure among large-band-gap solid insulators.

Under strong shock compression, the insulating/conducting transition is enhanced by the thermal promotion of electrons across the band gap.[6] This is a result of high temperatures produced by high-pressure (>100-GPa*) shock waves. A variety of materials has been shocked into conductive matter that is highly reflective at the shock front.[6–10] LiF has been previously observed to be transparent when shocked to ~115 GPa (Refs. 8 and 11) and becomes reflective for shock pressures >500 GPa (Ref. 6).

Recently, ramp compression has been used to compress materials to pressures above 100 GPa, while keeping the temperature low compared to that of a shock wave.[12] This work shows that LiF remains transparent when ramp compressed to 800 GPa—the highest pressure under which a transparent insulator has ever been observed. We use a new technique to measure its refractive index at pressures of 30 to 800 GPa. Early dynamic-compression experiments have shown the refractive index of various insulators to increase linearly with density at low pressure (~100 GPa). The results presented here indicate that the linearity of the LiF refractive index increase over a larger density range than previously shown. This is expected since the electronic polarizabilites of large-band-gap insulators typically increase with compression. The results presented here are the highest-pressure refractive-index measurements to date.

_____

*100 GPa = 1 Mbar

Ramp-compressed LiF remains transparent at higher pressures than in shock compression because thermal excitation is insufficient to produce conduction electrons. As a result, at these high compressions we expect that only the effects of density are important and use this to infer the pressure-induced band-gap closure of LiF using a single-oscillator model.[13] Extrapolation of those results, although crude, indicates that ramp-compressed LiF may remain transparent to greater than 4000 GPa, well above the Goldhammer–Herzfeld criterion for metallization (~2800 GPa) (Refs. 14–16). LiF will therefore continue to have technical utility as a diagnostic window for experiments at extreme pressures, and the predicted band-gap closure provides important estimates for band-structure calculations.

In the present work, the refractive index of LiF was measured using ramp compression to 800 GPa. Diamond pistons were ramp compressed using the OMEGA laser.[17] Diamond targets consisted of two sections: a free surface and a LiF window mounted on half of the rear surface. VISAR measurements were made at both sections to determine the refractive index. The subsequent sections discuss the relevant theory regarding the measurement technique, followed by a discussion of the experimental method and the experimental results. In the final section, an effective-oscillator model is used to interpret the results, providing an estimation of the band-gap closure.

Theory

In many high-pressure experiments, the motion of a reflecting interface behind an optical window is detected by measuring Doppler shifts with a velocity interferometry system for any reflector (VISAR).[18] The reflected probe beam passes through the compression wave in the window, so the observed Doppler shift depends on the refractive index of the compressed window material. LiF is frequently used as an optical window because its transparency at high pressure allows one to make *in-situ* measurements of samples confined by that window.[8,11] Hayes[19] showed that for unsteady compression waves in windows, the *true* (U_t) and *apparent* (U_a) interface velocities (viewed through the compressed window) are directly related to the density-dependent refractive index of the window as

$$\frac{dU_a}{dU_t}\Bigg|_{U_t} = \left(n - \rho \frac{dn}{d\rho}\right)\Bigg|_{U_t} = f(\rho), \qquad (1)$$

where the density (ρ) and refractive index (n) are evaluated as functions of U_t. One can show that this gives $n(\rho)$ explicitly as

$$n(\rho) = \rho \left[\frac{n_0}{\rho_0} - \int_{\rho_0}^{\rho} \frac{f(\rho')}{\rho'^2} d\rho'\right]. \qquad (2)$$

In this work, $U_a(U_t)$ was measured using diamond as an impedance-matching standard and the refractive index as a function of density was determined by solving Eq. (2).

Experimental Method

The targets consisted of a planar diamond piston with two sections: half a free surface and an LiF window attached to the second half [see inset of Fig. 126.9(a)]. Planar compression waves, driven by direct laser ablation, produced identical compression waves across the two sections (bare and LiF) of the piston. The free-surface (bare diamond) velocity (U_{fs}) and the *apparent* interface (diamond–LiF) velocity (U_a) were measured simultaneously using VISAR.[18] The response of the free surface was used to infer the *true* velocity of the piston/window interface.

The method of characteristics[20] was used to determine the drive-pressure history applied to the target by propagating U_{fs} backward to the loading surface. The free-surface wave profile, shown in the inset of Fig. 126.9(a), displays a distinct plateau at 2 μm/ns caused by the drop from the longitudinal to the bulk sound speed as the elastic limit of diamond was exceeded. In this experiment, as in previous experiments,[12] the plateau showed a very constant velocity and the elastic limit was treated as a straightforward drop in the sound speed. Using that assumption, the calculated drive pressure was determined and then forward propagated to the diamond/LiF boundary, where pressures were impedance matched, thereby determining U_t. The diamond-ramp wave response measured by Bradley *et al.*,[12] which includes diamond strength, and the *SESAME* Table 7271 (Ref. 21) for LiF were used. The LiF *SESAME* Table 7271 accounts for hydrostatic deformations while neglecting plastic deformations. The inclusion of a Steinberg–Guinan[22,23] strength model in the LiF equation of state (EOS) influenced the calculated interface pressure by ≪1% prior to peak compression. As Ao *et al.*[22] have shown, plastic effects in the interface velocity are of consequence only after peak compression. Analysis is terminated when interface yielding or "pullback" is observed, corresponding to ~5.5 ns for the inset of Fig. 126.9(b). LiF strength effects were neglected since the error contribution was significantly less than other sources.
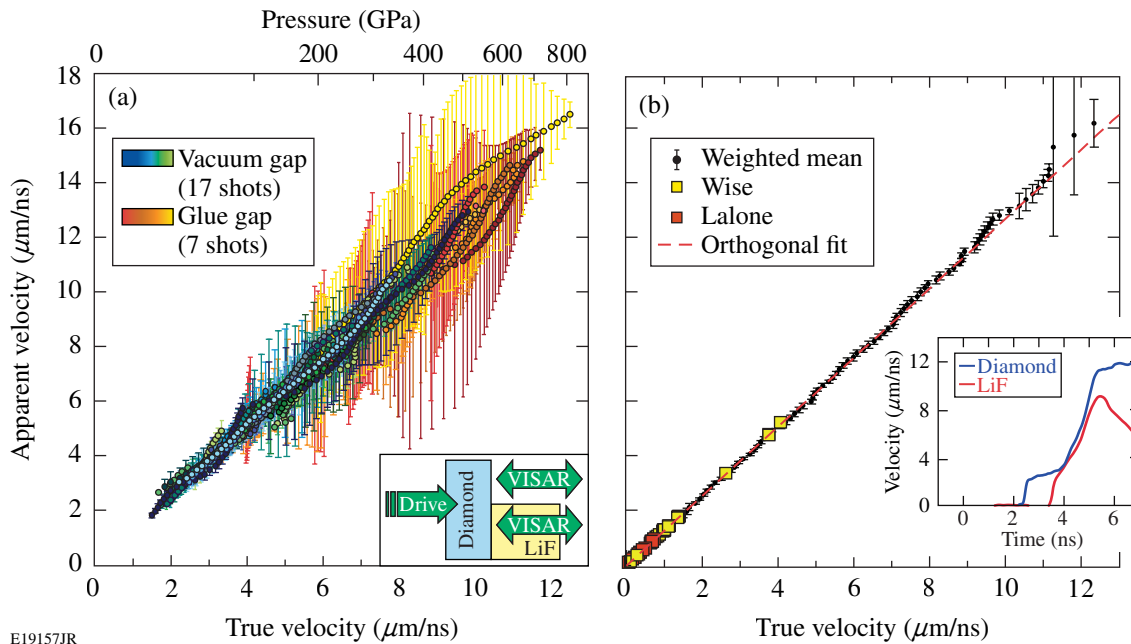

Figure 126.9
(a) *Apparent* and *true* velocity measurements for all experiments. Vacuum-gap and glue-gap experiments are distinguished by their corresponding colors. Inset shows the target diagram. (b) Weighted average of all shots. Orthogonal regression and previous shock data are included.[8,11] Inset shows the VISAR measurements from a single experiment.

E19157JR

The experiments were performed on the OMEGA Laser System.[17] The ablation pressure was controlled by temporal shaping the drive laser pulse to produce compressions in LiF from 30 to 800 GPa. These drive pulses compressed the targets without creating shock waves in either the chemical-vapor-deposition (CVD) diamond pusher or LiF samples over the duration of the experiment.

Laser intensity scaled as $\sim t^3$ for pulse-shape durations of 4 to 7 ns. The diamond thickness for those experiments was 46 μm (± 1 μm) and 100 μm (± 3 μm), respectively. A 500-μm-thick, high-purity LiF window was mounted over half of the rear of these diamond targets oriented with the $\langle 100 \rangle$ axis along the pressure-loading direction. Samples were glued at the edges such that the compressed diamond released directly into the LiF where there was no glue. A 1000-Å titanium coating was applied to the diamond/LiF interface to increase the reflectivity for interferometer measurements. Three targets were constructed with gold layers (3 to 5 μm thick) placed 10 to 15 μm from the ablation surface to act as an x-ray shield to ensure there was no effect from high-energy x rays passing through the target. No difference was observed in the results from targets with and without these shields.

Experimental Result

1. Wave Profile Analysis

A total of 17 shots was performed to determine the *true* and *apparent* velocities as described above. Each of the 17 continuous measurements is shown as an ensemble of like-colored points in Fig. 126.9(a). The measured *apparent* velocities were observed to monotonically increase with pressure with no observed discontinuities, indicating a single phase of LiF existed to 800 GPa. This is consistent with recent *ab-initio* calculations performed by Smirnov.[24] The pressures corresponding to these velocities were determined from the LiF *SESAME* EOS[21] as shown on the top axis. In those experiments, a weak shock was initiated in the LiF window; this was treated as an initial characteristic whose parameters were determined from impedance matching with the Hugoniot. The effect of shock formation in the LiF window is examined in **LASNEX Simulations** (p. 63).

Seven additional targets employed ~ 2 μm of glue to fill the gap between the diamond and the LiF. At low pressures, the compressibility of the glue (and reverberations within it) caused the data to deviate from the targets with no glue between the LiF window and diamond. Once the glue "rang up" to higher pressure, the data followed the trend of targets with no glue-filled gap. Simulations indicated that after the glue rang up, corrections for the presence of ~ 2-μm gaps caused a shift of the *true* particle-velocity profiles after gap closure by ~ 3 ps, much less than the timing accuracy of these experiments.

The dominant errors in these calculations resulted from the precision of fringe-shift measurements (2.5% of a fringe) and uncertainty in the diamond isentrope cited by Bradley *et al.*[12] Measurements published by Hicks *et al.*,[6] which were later re-examined by Celliers *et al.*,[25] are the only high-pressure measurements for LiF above 500 GPa published to date. Comparison of measurements made by Hicks *et al.*[6] at ~ 1400 GPa with the *SESAME* Table 7271 indicates an $\sim 7\%$ error in pressure; therefore, a 10% error in pressure is assumed for the LiF isentrope.[22] The errors in the timing correlation between U_a and U_t was of the order of 47 ps and 93 ps for cameras 1 and 2, respectively,[18] corresponding to uncertainties added in quadrature of the etalon delay (37 ps and 78 ps) and nonuniformity in the drive planarity (5 pixels at sweep rates of 6 ps/pixel and 10 ps/pixel). Systematic uncertainties are attributed to camera shear (6 and 10 ps), gap correction ~ 1 ps (33% of the calculated temporal shift), and the neglect of LiF material strength ($\ll 1\%$ change in peak interface pressure). Systematic uncertainties are estimated to be 5% of the total uncertainty and therefore neglected. Random errors were propagated through the method of characteristics using a Monte Carlo procedure that propagates uncertainties randomly chosen from a normal distribution.[26]

Steep gradients in the measured velocity profiles account for the large errors observed for single shots in Fig. 126.9(a). These were reduced by using a ramp compression that rose more gradually, albeit to lower pressures. Streaked optical pyrometer[27] measurements of LiF were dominated by thermal emission from the diamond anvil observed through the LiF. Comparison of the self-emission from the diamond-free surface and the diamond/LiF interface suggests that the LiF window temperature remained below 1000 K for all cases.

Figure 126.9(b) shows the weighted mean (black points) of the data from Fig. 126.9(a) using the associated errors discussed above. The large errors between 700 to 800 GPa occur because only a single experiment reached those pressures. The dashed line is the linear portion of a fit performed to that weighted mean (see below). Shock-wave data taken from Wise and Chhabildas[8] and LaLone *et al.*[11] are shown up to 115 GPa as yellow and red squares, respectively.

A second-order orthogonal polynomial regression[25,26] was to fit the U_t [km/s] and U_a [km/s] particle velocities: $U_a(U_t) = a_0 + a_1 (U_t - \beta) + a_2 (U_t - \gamma_1)(U_t - \gamma_2)$, where $\beta = 2.41$ km/s, $\gamma_1 = 0.713$ km/s, and $\gamma_2 = 9.53$ km/s were determined by the distribu-

tion of U_t in the data being fit. Since these parameters depend on the independent variable, errors were not assigned. Coefficients (a_0, a_1, and a_2) were determined from a weighted χ^2 minimization. In the orthogonal fit, the value of each coefficient is independent of higher-order terms, diagonalizing the co-variance. U_t is considered the independent variable and U_a the dependent one with a standard deviation $\sigma_{U_a}^2 = (\delta U_a)^2 + (1.28\,\delta U_t)^2$. δU_a is the error associated with the measured interface velocity and δU_t is the error determined by Monte Carlo simulations, which is weighted by 1.28 to account for the estimated slope. Errors determined in the orthogonal fitting coefficients underestimate deviations observed within the data. This was observed when shots were removed at random and orthogonal fitting was performed. Coefficient errors were determined by standard deviations calculated from 100 discrete shot groupings of the 24 experiments: $a_0 = 3.0634$ [km/s], $a_1 = 1.2751\pm0.0082$, and $a_2 = 0.0008\pm0.0015$ [s/km]. Errors were not assigned to a_0 since it represents the centroid of the data. The slope (a_1) dominates the determination of the refractive index [Eq. (1)], and contributions from the curvature (a_2) are assumed negligible because of their relative size and the bounding of zero.

Equation (2) was used to calculate $n(\rho)$ (Fig. 126.10) using the weighted mean (black line). The refractive index and density under standard conditions (1.3935 and 2.6380 g/cc) were used as the boundary. The refractive index determined from the orthogonal fitting parameters is

$$n = 1.275(\pm0.008) + 0.045(\pm0.003)\rho, \tag{3}$$

where the second-order term (a_2) has been neglected. The results obtained are in agreement with high-precision shock results up to 20 GPa (Ref. 11)

$$n = 1.277(\pm0.002) + 0.0443(\pm0.008)\rho, \tag{4}$$

and diamond-anvil experiments[28]

$$n = 1.25(\pm0.03) + 0.05(\pm0.01)\rho. \tag{5}$$

The effective polarizability (α) of LiF is calculated using the Clausius–Mossotti relation

$$\frac{1}{\rho}\frac{\varepsilon-1}{\varepsilon+2} = \frac{4\pi N_A}{3}\alpha, \tag{6}$$

where ε is the dielectric function and N_A is Avogadro's number. For these experiments, the LiF absorption was negligible, indicating that the imaginary part of the refractive index was small or $\varepsilon \approx n^2$. Using Eq. (6) and this approximation, the
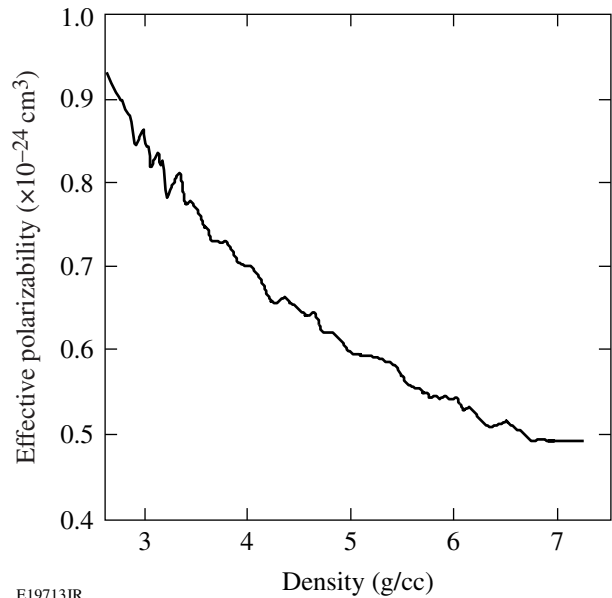
effective polarizability is calculated and plotted as a function of compression in Fig. 126.11. The effective polarizability is observed to decrease with increasing pressure.
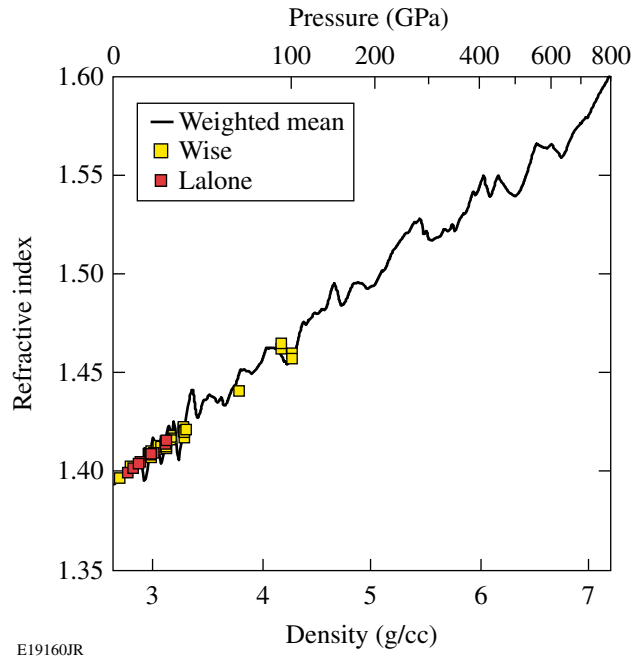
E19160JR

Figure 126.10
Refractive index as a function of density determined using the weighted average and linear orthogonal fit. Previous data shock is included.[8,11]

E19713JR

Figure 126.11
The effective polarizability determined from the Lorentz–Lorenz relation plotted as a function of density.

2. LASNEX Simulations

LASNEX[29] simulations were performed to address concerns regarding shock formation in the LiF window and LiF material strength. The arrival of the diamond elastic limit (EL) in the LiF window generates a weak shock. Compression waves in the LiF window may reflect off the shock front, and the arrival of those waves at the LiF would violate the conditions required in the derivation of Eq. (1) (Ref. 19). Since the method of characteristics does not account for the potential of shock formation, LASNEX simulations were performed to verify the characteristic calculations. LASNEX calculations used a diamond EOS with a Steinberg–Guinan–strength model to recover the EL[23] and LiF *SESAME* Table 7271 (Ref. 21). The pressure drive was applied 10 μm inside the front surface to account for the material ablated by the laser driver. This applied pressure is estimated to best match the measured diamond free-surface velocity.

LASNEX simulations were performed on shot 56113, and the results are shown in Figs. 126.12(a) and 126.12(b). Figure 126.12(a) contains a plot of the diamond free-surface velocity measured using VISAR (blue) and the estimated velocity determined from LASNEX (black) for an approximate applied laser intensity. Figure 126.12(a) shows that the LASNEX free-surface velocity correlates well with the measured free-surface velocity. The applied pressure drive that determines the free-surface velocity is then used to simulate the *true* interface velocity. The noticeable discrepancies between the LASNEX simulation and measure free-surface velocity at 3.9 ns and 4.2 ns is due to the limitations of Steinberg–Guinan–strength model. That model predicts a higher EL than observed in this study generating the noticeable two-wave structure. As observed by McWilliams *et al.* the diamond EL varies and these variations are the cause of the observed discrepancy.[30]

Figure 126.12(b) compares interface velocities calculated using both methods. The LASNEX-predicted *true* interface velocity (black) and the *true* interface velocity calculated using the method of characteristics (red) infer nearly identical velocities prior to peak compression. The excellent agreement indicates that either (a) shock formation does not occur in the LiF window or (b) the effects of shock formation under these conditions do not significantly perturb the interface velocity prior to peak compression. This indicates that the requirements on Eq. (1) are met and Eq. (1) remains valid for these experiments. Furthermore, simulations performed with and without a Steinberg–Guinan–strength model differ ≪1% in pressure.

Discussion

The temperatures achieved in this study are significantly lower than temperatures for identical pressures along the principal Hugoniot. *SESAME* Table 7271 predicts the principal isentrope temperature at 400 GPa and 800 GPa to be ~700 k and ~800 k, respectively. The temperature along the principal Hugoniot for those pressures are significantly higher (12,500 k and 31,500 k). Molecular dynamic simulations[31] suggest that the Hugoniot approaches the melt line at ~150 GPa at ~3500 k. Quantum molecular dynamics simulations predict as LiF melts, it transitions from a large gap insulator into a reflective material and during this transition develops a nonlinear refractive index.[32] The low temperatures achieved in this study prevent LiF from approaching melt, inhibiting the development of a nonlinear refractive index.

An effective-oscillator model[13] was used to interpret the observed linear dependence of refractive index on density. The effective-oscillator model describes optical properties as a weighted average over the visible spectrum. It is a simplistic dielectric model that predicts the magnitude and dispersion of
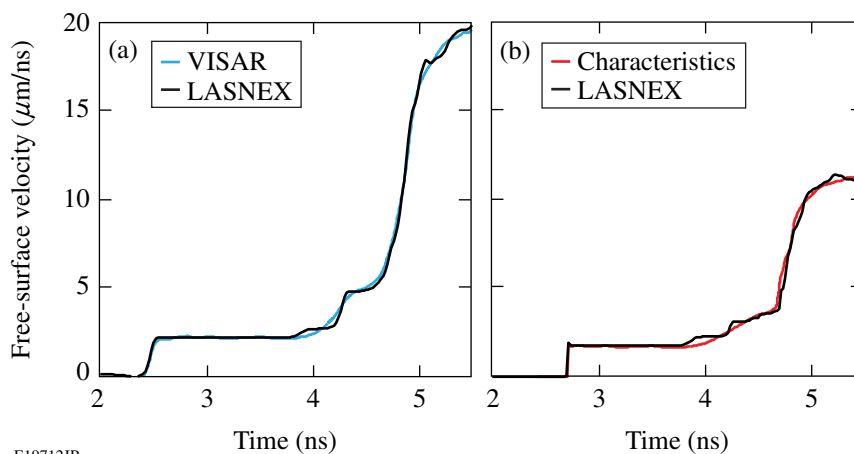

Figure 126.12
Comparison of hydrocode simulations and the method of characteristics for shot 56113. (a) LASNEX ablation pressure is determined by matching the LASNEX free-surface velocity (black) with VISAR measurement (blue). (b) The ablation pressure calculated using LASNEX is then used to determine the *true* interface velocity. Comparison of the LASNEX results (black) and the method of characteristics (red) is shown.

E19712JR

ionic and covalent substances. The refractive index is defined by two "average" parameters: the dispersion energy (E_d) and single-oscillator energy (E_0). E_0 is empirically related[13] to the lowest direct optical transition E_t defined as the excitonic or band gap. The single-oscillator energy represents an average energy gap where the direct and indirect gaps may be smaller or exceed that energy.[33]

Wemple and DiDomenico[13] have shown that frequency-dependent refractive index for covalent and ionic materials can be fit to

$$n^2 - 1 = \frac{E_d E_0}{E_0^2 - \hbar^2 \omega^2}, \tag{7}$$

where E_d is the dispersion energy, E_0 is the single-oscillator energy, and $\hbar\omega$ is the photon energy. In a survey of over 100 solid and liquid insulators at ambient conditions, this model fits the frequency-dependent refractive index well.[13]

This model was applied to the pressure-induced closure of the H_2 band gap over a large density range[34–36] and successfully predicted the emergence of excitonic absorption in the visible spectrum.[4] Those studies show the H_2 exciton shifts from 14.5 eV to 2 eV with a slightly sublinear dependence on density over nearly 15-fold compression. The effective-oscillator model has been applied to H_2O ice, demonstrating a linear reduction in the band gap over 2.3-fold compression.[33] In that study, the dispersion was measured from 569 to 741 nm at pressures ranging from 0 to 120 GPa. At discrete pressures, the effective-oscillator parameters (E_d and E_0) were determined. Zha et al.[33] found that E_d was independent of density (remained constant) and that the effective gap closed monotonically with density. Wemple and DiDomenico[13] have shown that the ratio of the band-gap energy to the lowest direct optical transition E_0/E_t is constant for constant dispersion energy (E_d).

The effective-oscillator model was applied to the data presented here, where the ambient values of E_d and E_0 were determined by fitting the refractive index to measured values in the range of 332 nm $< \lambda <$ 732 nm, i.e., the wavelength region near the probe laser.[16] Fixing E_d to its ambient value, E_0 is calculated as a function of density using Eq. (7), as shown in Fig. 126.13. For the alkali halides of NaCl structure, the average ratio of single-oscillator energy to direct band gap is $E_0/E_t = 1.36$. This effective band gap begins at the intense exciton observed at ambient pressure[37] and then decreases with rising pressure.

Extrapolation of these results (a crude approximation) indicates that the band gap may close above >4000 GPa. This suggests that LiF will remain transparent well above the Goldhammer–Herzfeld (G–H) criterion (~2800 GPa) (Refs. 14–16). This difference is consistent with the observed behavior of He and Ne, which exhibited abnormally high metallization at pressures 10× greater than predicted by the G–H criterion.[5,38]
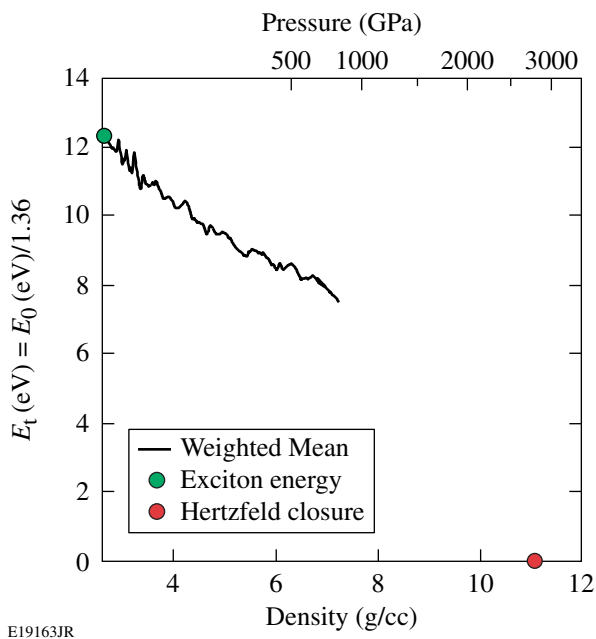

E19163JR

Figure 126.13
Density dependence of the single-oscillator model (E_t). Extrapolation suggests that LiF may remain transparent to pressure above 4000 GPa.

Conclusion

Direct laser ablation was used to ramp compress LiF from 30 to 800 GPa. LiF was observed to remain transparent over this pressure range; this is the highest-pressure insulator ever observed. The apparent and true particle velocities were measured over this range and were used to calculate the refractive index of compressed LiF, which was found to depend linearly on density. These are the highest pressure measurements of refractive index to date and are used to infer the pressure-induced band-gap closure of compressed LiF using an effective-oscillator model. These measurements provide a VISAR correction factor up to 800 GPa. Extrapolation of these results suggests that LiF remains transparent to pressures >4000 GPa as long as the temperature remains sufficiently low. If true, LiF will prove to be a valuable window for extremely high pressure ramp-compression experiments.

REFERENCES

1. R. Reichlin *et al.*, Phys. Rev. Lett. **56**, 2858 (1986).

2. K. A. Goettel *et al.*, Phys. Rev. Lett. **62**, 665 (1989).

3. R. Reichlin *et al.*, Phys. Rev. Lett. **62**, 669 (1989).

4. P. Loubeyre, F. Occelli, and R. LeToullec, Nature **416**, 613 (2002).

5. J. C. Boettger, Phys. Rev. B **33**, 6788 (1986).

6. D. G. Hicks *et al.*, Phys. Rev. Lett. **91**, 035502 (2003).

7. S. B. Kormer, Sov. Phys.-Usp. **11**, 229 (1968).

8. J. L. Wise and L. C. Chhabildas, Sandia National Laboratory, Albuquerque, NM, Report SAND-85-0310C, NTIS Order No. DE85015505 (1985).

9. D. K. Bradley *et al.*, Phys. Rev. Lett. **93**, 195506 (2004).

10. J. Eggert, S. Brygoo, P. Loubeyre, R. S. McWilliams, P. M. Celliers, D. G. Hicks, T. R. Boehly, R. Jeanloz, and G. W. Collins, Phys. Rev. Lett. **100**, 124503 (2008).

11. B. M. LaLone *et al.*, J. Appl. Phys. **103**, 093505 (2008).

12. D. K. Bradley *et al.*, Phys. Rev. Lett. **102**, 075503 (2009).

13. S. H. Wemple and M. DiDomenico, Jr., Phys. Rev. B **3**, 1338 (1971).

14. A. Goldhammer, in *Monatshefte für Mathematik* (Teubner, Leipzig, Berlin, 1913), Vol. 27.

15. K. F. Herzfeld, Phys. Rev. **29**, 701 (1927).

16. E. M. Bass, ed. *Handbook of Optics*, 2nd ed., Volume II: Devices, Measurements, and Properties (McGraw-Hill, New York, 1994).

17. T. R. Boehly, D. L. Brown, R. S. Craxton, R. L. Keck, J. P. Knauer, J. H. Kelly, T. J. Kessler, S. A. Kumpan, S. J. Loucks, S. A. Letzring, F. J. Marshall, R. L. McCrory, S. F. B. Morse, W. Seka, J. M. Soures, and C. P. Verdon, Opt. Commun. **133**, 495 (1997).

18. L. M. Barker and R. E. Hollenbach, J. Appl. Phys. **43**, 4669 (1972).

19. D. Hayes, J. Appl. Phys. **89**, 6484 (2001).

20. J. R. Maw, AIP Conf. Proc. **706**, 1217 (2004).

21. S. Crockett and S. Rudin, Los Alamos National Laboratory, Los Alamos, NM, LA-UR-06-8401 (2006).

22. T. Ao *et al.*, J. Appl. Phys. **106**, 103507 (2009).

23. D. J. Steinberg, S. G. Cochran, and M. W. Guinan, J. Appl. Phys. **51**, 1498 (1980).

24. A. Smirnov, Phys. Rev. B **83**, 014109 (2011).

25. P. M. Celliers *et al.*, J. Appl. Phys. **98**, 113529 (2005).

26. P. R. Bevington and D. K. Robinson, *Data Reduction and Error Analysis for the Physical Sciences*, 3rd ed. (McGraw-Hill, Boston, 2003).

27. J. E. Miller, T. R. Boehly, A. Melchior, D. D. Meyerhofer, P. M. Celliers, J. H. Eggert, D. G. Hicks, C. M. Sorce, J. A. Oertel, and P. M. Emmel, Rev. Sci. Instrum. **78**, 034903 (2007).

28. N. M. Balzaretti and J. A. H. Da Jornada, J. Phys. Chem. Solids **57**, 179 (1996).

29. G. B. Zimmerman and W. L. Kruer, Comments Plasma Phys. Control. Fusion **2**, 51 (1975).

30. R. S. McWilliams, J. H. Eggert, D. G. Hicks, D. K. Bradley, P. M. Celliers, D. K. Spaulding, T. R. Boehly, G. W. Collins, and R. Jeanloz, Phys. Rev. B **81**, 014111 (2010).

31. R. Boehler, M. Ross, and D. B. Boercker, Phys. Rev. Lett. **78**, 4589 (1997).

32. J. Clérouin *et al.*, Phys. Rev. B **72**, 155122 (2005).

33. C.-S. Zha *et al.*, J. Chem. Phys. **126**, 074506 (2007).

34. J. van Straaten and I. F. Silvera, Phys. Rev. B **37**, 6478 (1988).

35. A. García *et al.*, Phys. Rev. B **45**, 9709 (1992).

36. R. J. Hemley, M. Hanfland, and H. K. Mao, Nature **350**, 488 (1991).

37. D. J. Mickish, A. B. Kunz, and T. C. Collins, Phys. Rev. B **9**, 4461 (1974).

38. S. A. Kairallah and B. Militzer, Phys. Rev. Lett. **101**, 106407 (2008).